

Study of multilayer systems in electron beam lithography

Robert Peters, Taras Fito, Luis Gutierrez-Rivera, Steven Dew, and Maria Stepanova^{a)}
Department of Electrical and Computer Engineering, University of Alberta, Edmonton, Alberta T6G 2V4, Canada and National Institute for Nanotechnology NRC, Edmonton, Alberta T6G 2M9, Canada

(Received 22 June 2013; accepted 17 October 2013; published 4 November 2013)

The authors investigate the influence of anticharging conductive layers on electron beam lithography (EBL) nanopatterning of polymethyl methacrylate (PMMA) resist on fused silica substrates both experimentally and numerically. They report simulations of EBL exposure and development accounting for the effects of different anticharging layers on top of PMMA resist and compare the predicted and fabricated nanopatterns on fused silica and on silicon substrates. © 2013 American Vacuum Society. [<http://dx.doi.org/10.1116/1.4827813>]

I. INTRODUCTION

Electron beam lithography (EBL) provides the current standard for high resolution nanofabrication. A number of emerging technologies, including nanophotonics, nanofluidics, nanobiosensors, nanoimprinting, and others, involve fabrication on alternative substrate materials compared to traditional materials, such as silicon wafers.^{1–8} Dielectric substrates, in particular, offer advantages of transparency and electrical insulating properties. Charging effects, however, become a significant hindrance to quality patterning on dielectric substrates due to beam defocusing, distortion, and displacement, limiting the resolution attainable using EBL processes employing polymeric resists.⁹

Inclusion of conductive layers has been shown to extend the capabilities of EBL for dielectric substrates by limiting the charging effects which degrade the pattern quality.^{10,11} These conductive layers, however, add an additional complexity to the fabrication process. Factors including layer thickness, grain formation, secondary electron generation, forward scattering, film conductivity, and heating of conductive layers may all play a role in the quality of EBL exposures for underlying resist layers. Simulation of exposure and development provides substantial benefit to understanding the various aspects involved in EBL fabrication at the deep nanoscale.^{12,13} In this work, we present a study of the EBL process for polymethyl methacrylate (PMMA) resist with conductive layers and extend our electron beam lithography simulation tool^{13,14} to incorporate the effects of such layers. Simulations of PMMA nanopatterning employing anticharging conductive layers are compared with the respective experiments.

II. EXPERIMENT

Fused silica (FS) was chosen in our experiments as a representative dielectric substrate due to its common use in a number of applications and ease of processing, and PMMA was employed as a positive tone resist. Although in various applications conductive layers can be placed above or below the resist layer,^{15–18} placement of the layers on top of the resist has the advantage of not affecting prior fabrication processes for multilayer devices. In this work, layers of

aluminum or aquaSAVE conductive polymer (Mitsubishi Rayon Co.) were placed on top of PMMA resist employing previously optimized processes as described in Ref. 18. In addition to FS substrates, control experiments were also conducted with silicon substrates to clarify how the inclusion of anticharging layers influences the EBL process in the absence of charging.

All samples were cleaned with either a piranha ($\text{H}_2\text{SO}_4:\text{H}_2\text{O}_2$, 3:1) solution or with an *N*-methyl-2-pyrrolidone based solvent followed by a thorough rinse in deionized water and drying in blown nitrogen. Both fused silica and silicon substrates were spin-coated with PMMA 950K with both pre- and postbakes at either 150 °C or 180 °C. AquaSAVE conductive polymer was placed by brushing of the polymer on top of the resist prior to spinning in order to ensure complete and uniform coverage. For deposition of aluminum, both magnetron sputtering and electron beam evaporation techniques were used. Deposition using a customized planar magnetron sputtering system (Kurt J. Lesker) using 80 W of power, and a set pressure of 70 mTorr, was found to damage the top layer of resist, resulting in up to a 20 nm reduction in resist thickness after development. In contrast, electron beam evaporation was not observed to have any noticeable impact on the resist layer. For this reason, only results obtained with evaporated aluminum films are reported here. Deposition of evaporated aluminum films was done with a deposition pressure of $\sim 7 \times 10^{-7}$ mTorr and a deposition rate of 0.02–0.03 nm/s for each sample using a Kurt J. Lesker water cooled bell jar evaporation system.

Arrays of dots of 100 nm pitch were exposed using a Raith 150^{TWO} system with 30 keV accelerating voltage and a 7.5 μm aperture. Arrays of 8.5 $\mu\text{m} \times 100 \mu\text{m}$ in size were separated by a minimum distance of 65 μm to eliminate proximity effect from surrounding arrays. Measurements of dots sizes were done in the center of each array for consistency of exposure conditions including the proximity effects within the arrays. After exposure, aluminum layers were removed using undiluted MF CD-26 developer (Microposit), with an estimated aluminum etch rate of 10 nm/min at room temperature. The samples were rinsed in deionized water and dried in nitrogen prior to development. Conductive polymer layers were removed using deionized water for 3 s without drying, followed by immediate development. Development was done at room temperature using an isopropyl alcohol (IPA):Water (7:3) mixture¹⁸ for 20 s. The

^{a)}Electronic mail: ms1@ualberta.ca

developed samples were analyzed systematically. Examples of developed PMMA samples with 7.5 fC/dot exposure dose are shown in Fig. 1. The thickness of the PMMA was verified with both Filmetrics and scanning electron microscope (SEM) measurements, and aluminum thicknesses were verified with SEM imaging and using an in situ quartz crystal microbalance thickness monitor. Imaging was done using a Hitachi S-4800 field emission SEM using a secondary electron detector after sputter coating samples with 3.5 nm of chrome to limit charging. Analysis of top down imaged dots was done using ImageJ software¹⁹ to measure the average dot diameters in PMMA on the various substrates.

III. THEORY

We simulate the EBL exposure and development processes using our original simulation tool described elsewhere.^{13,14} Our model of exposure in a positive-tone polymeric resist incorporates the scission of the resist's main chains due to inelastic collisions of primary, secondary, and backscattered electrons, see details in Refs. 13, 14, and 20. The simulation of exposure generates a detailed spatial distribution of the yield of main-chain scission in the resist, dependent on pattern design, dose, voltage, and substrate and resist material. The yield of scission subsequently is converted into local volume fractions of resist fragments of various lengths, which are employed to compute the resist development profile. Development profiles of the resist are attained using efficient kinetic approximations of the diffusion process. Development simulation involves, first, resist partitioning in a uniform 3D mesh, down to 1 nm resolution. A temperature dependent value of average fragment diffusivity is assigned to every cell of the mesh, and the corresponding local dissolution rate is computed. During each

simulation step, a cell or a group of cells at the resist-developer interface is dissolved, followed by updating the amount of remaining polymer. This process is repeated until a desired development time is reached. A more detailed description of the method and its validation can be found in Refs. 13, 14, and 21. Examples of simulated exposure and development profiles for a periodic dot pattern in 100 nm thick PMMA resist layer on a silicon substrate are shown in Figs. 2(a) and 2(b), respectively. The simulations shown in the figure were performed for 30 keV exposure voltage at a dose of 10 fC/dot, and development during 20 s in a 7:3 IPA:H₂O mixture at room temperature.

In this work, we extended our simulation model^{13,14} to include the influence of the anticharging layer on the distribution of the yield of scission in the resist. More specifically, we have accounted for primary electron beam broadening in the anticharging layer before the beam reaches the resist [Fig. 3(a)] as described below.

When a thin primary electron beam passes through a resist, the beam is broadened by elastic scattering, and the broadening increases with depth, z . In a uniform resist layer, the dependence of the beam broadening on depth is described by the well-known equation²²

$$F(\rho, z) = \frac{3\lambda}{z^3} \exp\left(-\frac{3\lambda\rho}{2z^3}\right)\rho, \quad (1)$$

where ρ is the lateral distance from the beam's initial axis and λ is transport free mean path of electrons in the resist, which depends on the beam energy and resist material properties. In our simulations, the value of λ is computed for given conditions of exposure according to the well-known model,²³ and subsequently, the primary beam distribution given by Eq. (1) is employed for convolutions with proper

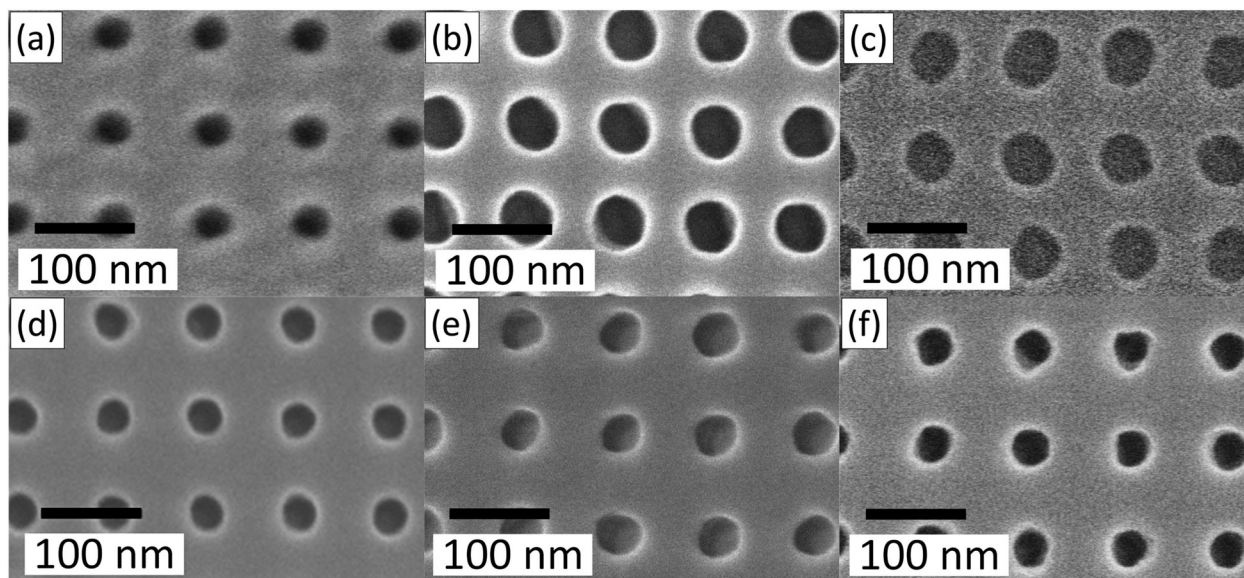


Fig. 1. SEM images of dots with a 100 nm pitch fabricated in 90–100 nm thick PMMA resist using 7.5 fC/dot exposure doses. All samples were exposed at 30 keV at the same dose and developed for 20 s in IPA:H₂O (7:3) at room temperature. (a)–(c) Fused silica substrates with (a) 70 nm of aquaSAVE conductive polymer, (b) 10 nm of evaporated aluminum conductive layer, and (c) 30 nm of evaporated aluminum conductive layer. (d)–(f) Silicon substrates with (d) 70 nm of aquaSAVE conductive polymer, (e) 10 nm of evaporated aluminum conductive layer, and (f) no conductive layer.

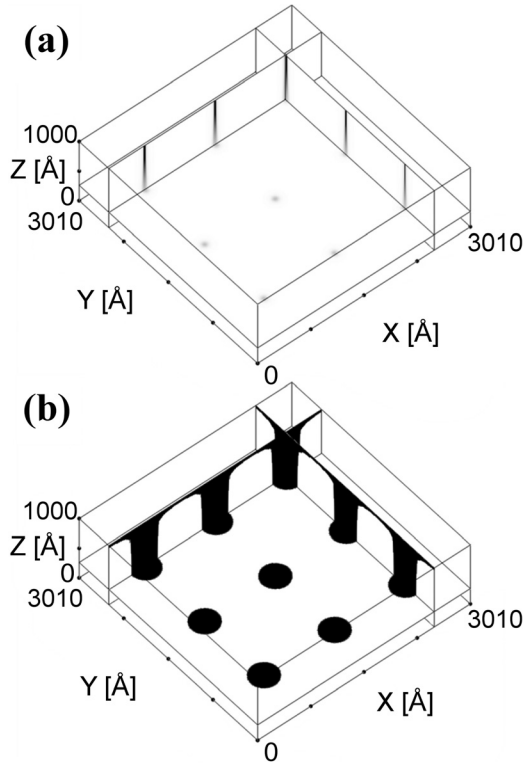


FIG. 2. (a) Simulated yield of main chain scission for a periodic dot array with a 100 nm pitch, in 100 nm thick PMMA resist on a silicon substrate using a 30 keV accelerating voltage and 10 fC/dot dose; (b) simulated development profile in the resist for the same conditions with 20 s development in IPA:H₂O (7:3), where the dark regions represent removed resist.

distributions of secondary and backscattered electrons,^{13,14} thereby determining the spatial distribution of the scission yield in the resist. To account for the anti-charging layers, we replaced Eq. (1) with a modified model of the beam broadening that we obtained employing an extension of the derivation described in Ref. 22.

According to Ref. 22, the probability that a charged particle traversing a distance z in a medium is found at a lateral distance between x and $x + dx$ from its initial direction due to scattering, wherein a corresponding net change of direction angle is between θ and $\theta + d\theta$, can be described by

$$F_{\lambda}(x, \theta, z) dx d\theta = \frac{\sqrt{3}\lambda}{\pi z^2} \times \exp\left(-\frac{2\lambda}{z}\left(\theta^2 - 3\frac{\theta x}{z} + 3\frac{x^2}{z^2}\right)\right) dx d\theta. \quad (2)$$

Integrating Eq. (2) over angle θ (Ref. 22) provides the probability to find a particle at a distance x from its initial direction

$$F_{\lambda}(x, z) dx = \frac{\sqrt{3}\lambda}{\sqrt{2\pi}z^3} \exp\left(-\frac{3\lambda x^2}{2z^3}\right) dx. \quad (3)$$

Because the probability in Eq. (3) does not depend on the lateral direction, it also can be represented by

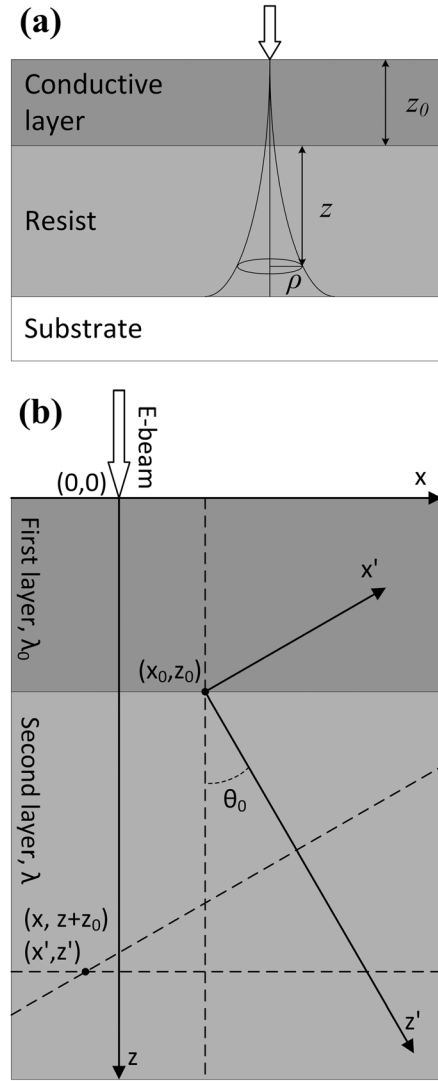


FIG. 3. (a) Schematic of beam broadening in a bilayered system; (b) schematic of notations used in the derivation of beam broadening Eq. (9).

$$F_{\lambda}(x, y, z) dx dy = F_{\lambda}(x, z) dx F_{\lambda}(y, z) dy = \frac{3\lambda}{2\pi z^3} \exp\left(-\frac{3\lambda(x^2 + y^2)}{2z^3}\right) dx dy. \quad (4)$$

By converting Eq. (4) into polar coordinates and integrating over the angular variable, the well-known Eq. (1) can be obtained.²² The derivation assumes that the deviation from the primary beam direction is small and that the majority of scattering events leading to beam broadening are elastic.

The described derivation can be easily extended to the case of a two-layered system. In this case, a narrow electron beam enters the first layer with a thickness z_0 and undergoes scattering described by the material's transport mean free path, λ_0 . The scattered beam penetrates into the second layer, where it is also scattered with a corresponding transport mean free path λ [see Fig. 3(b)]. In order to compute the distribution of primary electrons at depth z in the second layer, we consider the contribution of the beam fraction passing through point (x_0, z_0) on the interface of the first and second

layer in the direction θ_0 and reaching point $(x'z')$ in the second layer, such that

$$x' = (x - x_0)\cos\theta_0 - z\sin\theta_0, \quad (5)$$

$$z' = (x - x_0)\sin\theta_0 + z\cos\theta_0. \quad (6)$$

In the small-angle approximation, these equations take a simpler form

$$x' = (x - x_0) - z\theta_0, \quad z' = z. \quad (7)$$

Summing over all initial positions x_0 and directions θ_0 we obtain

$$\begin{aligned} F(x, z + z_0) &= \int_{-\infty}^{\infty} dx_0 \int_{-\infty}^{\infty} d\theta_0 F_{\lambda_0}(x_0, \theta_0, z_0) F_{\lambda}(x - x_0 - z\theta_0, z) \\ &= \sqrt{\frac{3\lambda}{2\pi}} \sqrt{\frac{1}{\frac{\lambda}{\lambda_0}(z + z_0)^3 + \frac{\lambda_0 - \lambda}{\lambda_0}z^3}} \exp\left(-\frac{3\lambda x^2}{2\left(\frac{\lambda}{\lambda_0}(z + z_0)^3 + \frac{\lambda_0 - \lambda}{\lambda_0}z^3\right)}\right). \end{aligned} \quad (8)$$

As a result, the beam broadening at depth z in the second layer is described by the following equation:

$$\begin{aligned} F(\rho, z) &= \frac{3\lambda}{\frac{\lambda}{\lambda_0}(z + z_0)^3 + \frac{\lambda_0 - \lambda}{\lambda_0}z^3} \\ &\times \exp\left(-\frac{3\lambda\rho^2}{2\left(\frac{\lambda}{\lambda_0}(z + z_0)^3 + \frac{\lambda_0 - \lambda}{\lambda_0}z^3\right)}\right) \rho. \end{aligned} \quad (9)$$

Figure 4 shows examples of the primary electron beam widths, according to Eq. (9), for PMMA resist covered by aluminum layers of 10 nm and 30 nm thicknesses, and for single layers of both PMMA and aluminum. As one could expect, the beam spread is significantly broader in a single

aluminum layer than with a single PMMA layer of similar thickness, and in two-layered samples the spread increases with the increased relative aluminum layer thickness. Further examples for the beam spread with other relative thicknesses of aluminum and PMMA layers can be found in Fig. S1 (supplementary material²⁴).

When simulating exposures of PMMA with an anticharging layer on top of the resist, we replaced Eq. (1) with Eq. (9) that accounts for the primary beam broadening in the added layer. Equation (9) is used for convolutions with the distributions of secondary and backscattered electrons, and the result is employed to compute the distribution of the scission yield.^{13,14,21} During the exposure simulations, electrostatic effects such as accumulation of charge in insulating substrates are not taken into account. Assuming that electron transport and scattering in the resist are not influenced by residual electrostatic charge, the simulations provide a “best-case” prediction of exposure with completely eliminated charging. When simulating development of exposed PMMA, we assume that the conductive layer is first removed without impacting the resist dissolution at the development stage.

Figures 5(a) and 5(b) depict an example of the simulations for a 100 nm thick PMMA on fused silica substrate with a 70 nm aquaSAVE layer, exposed by 30 keV electrons with a 10 fC/dot dose and developed during 20 s at room temperature in a 7:3 IPA:H₂O mixture. In comparison with Fig. 2(a) where a similarly processed sample on a silicon substrate without a conductive layer is shown, the distribution of the scission yield in Fig. 5(a) exhibits a more pronounced broadening of the beam, and the resulting dot diameters after development [Fig. 5(b)] are somewhat larger than in Fig. 2(b).

The diameter of simulated dots after development was used for characterizing the influence of various anticharging layers. As can be seen in Fig. 5(b), the predicted diameter of dots varies slightly with depth. In order to accurately compare the predicted dot diameters with top-down SEM experimental images, the dot diameters were measured at the depth where the dots are the narrowest.

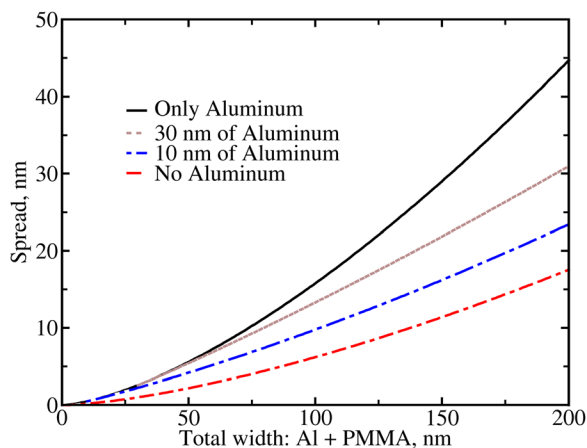


Fig. 4. (Color online) 30 keV primary electron beam spread at the surface of substrate, for a PMMA resist covered by aluminum layers of 10 nm and 30 nm thicknesses, and for single layers of PMMA and aluminum of various thicknesses. The beam spread is defined as a distance from the initial direction where the electron density is approximately 22% of the maximum density value.

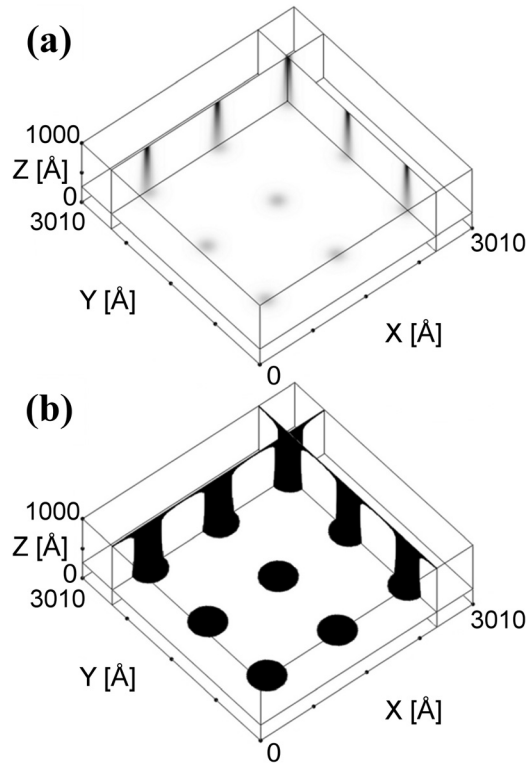


FIG. 5. (a) Simulated yield of main chain scission for a periodic dot array with 100 nm pitch, in 100 nm thick PMMA resist on a fused silica substrate with 70 nm of aquaSAVE conductive polymer on top of the resist (not shown) using a 30 keV accelerating voltage with 10 fC/dot dose; (b) simulated development profile for the same conditions with 20 s development in IPA:H₂O (7:3) at room temperature. The color scheme is as in Fig. 2.

In this paper, we focus on the simulations of uniform periodic dot arrays with 100 nm pitch and exposed with a range of doses (1–20 fC/dot) with a 30 keV voltage in 100 nm thick PMMA layers. However, for the sake of generality, in Figs. S2–S5 (supplementary material) we have also presented simulation results for different thicknesses of resist and exposure voltages.

IV. RESULTS AND DISCUSSION

Patterned samples with 100 nm pitch dot arrays in PMMA on fused silica and silicon substrates were fabricated employing EBL exposures at a range of doses over micron scaled areas to evaluate the effectiveness of anti-charging layers. 100 nm pitch dot arrays offered a suitable process window and latitude to investigate the dependence of dose on the quality of the periodic features. Here, we used fused silica as a dielectric substrate and silicon wafers as a benchmarking material. Conductive layers of either aquaSAVE conductive polymer or aluminum were used to compare their respective effects. Below we describe the different combinations of conductive layers with substrates and compare our experimental results with the theoretical predictions.

Figure 6 compares the measured and predicted diameters of dots in 100 nm thick PMMA resist on the various substrates with 70 nm aquaSAVE anticharging layers. The figure also presents benchmark experimental and numerical results for PMMA patterning on silicon substrates without a

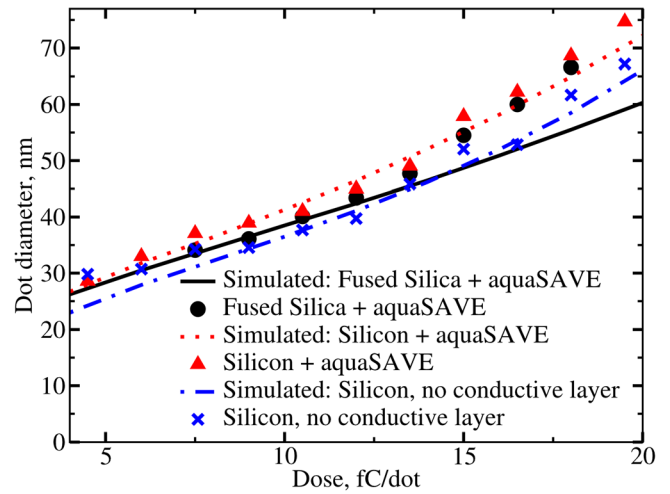


FIG. 6. (Color online) Comparison of dot sizes for 100 nm pitch dot arrays in 100 nm thick PMMA for a range of exposure doses on silicon and fused silica substrates using a 30 keV accelerating voltage and 20 s development in IPA:H₂O (7:3). Lines correspond to simulated results and symbols correspond to experimental data.

conductive layer. Analysis of simulations indicates that inclusion of a 70 nm aquaSAVE layer on top of the resist leads to wider spatial distributions of the yield of scission, accompanied by an approximately 75% decrease in the scission yield at the resist–substrate interface, which explains the trends seen in Fig. 6. It can also be seen that these benchmark experiments exhibit very good agreement with the corresponding simulations, as expected. The addition of the conductive polymer layer tends to increase the dot diameter by 3–10 nm depending on the dose.

High quality patterning of dot arrays was obtained on fused silica substrates using aquaSAVE conductive polymer [see Fig. 1(a)]. Comparison of samples using aquaSAVE layers on both fused silica and silicon showed similar dot diameters for the same doses (see Fig. 6). This demonstrates not only the effectiveness of conductive polymers in providing high resolution patterning on dielectric substrates but also allows for similar exposure dose requirements with both substrates. Another observation, as can be inferred from Figs. 1(a), 1(c), and 6, is that the average dot diameters showed only moderate increase due to the presence of a 70 nm aquaSAVE layer in comparison with benchmark experiments on silicon substrates without the anti-charging layer. This also demonstrates that the conductive polymer both effectively provides good conductivity as well as enables high resolution nanopatterning on dielectric substrates.

Simulation and experimental results presented in Fig. 6 match closely for the aquaSAVE layer, supporting the validity of our theoretical model for multilayered systems. It seems that indeed the major factor influencing the morphology of the developed resist with the conductive polymer layer is the beam broadening due to forward electron scattering in the layer.

Figure 7 compares the measured and simulated dot diameters in PMMA on fused silica substrates with evaporated aluminum anticharging layers, and the corresponding SEM images are shown in Figs. 1(b) and 1(c). As it can be seen in

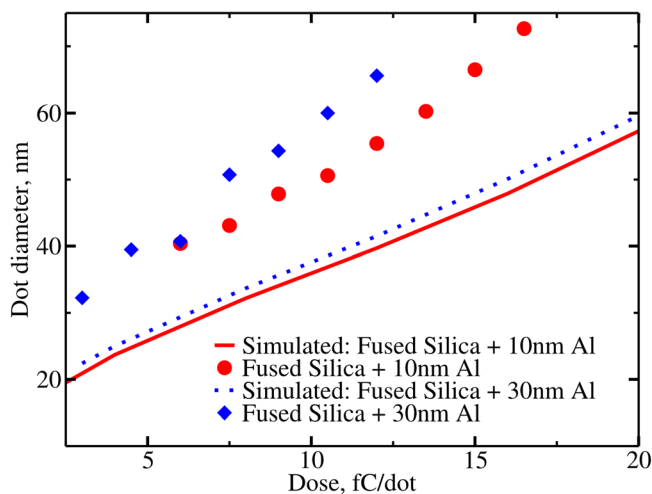


Fig. 7. (Color online) Comparison of dot sizes for 100 nm pitch dot arrays in 100 nm thick PMMA for a range of exposure doses on fused silica, using a 30 keV accelerating voltage and 20 s development in IPA:H₂O (7:3). Lines correspond to simulated results and symbols correspond to experimental data.

the figures, high quality dot arrays were obtained on samples of fused silica with aluminum anticharging layers of both 10 nm and 30 nm thickness. However, in comparison with samples using conducting polymer, 10 nm thick aluminum anticharging layers resulted in larger dot diameters at similar processing conditions. The dot diameters were also larger than predicted by simulations for Al films (Fig. 7). Increasing the thickness of the aluminum layer from 10 nm to 30 nm did not eliminate the discrepancy, but gave even larger features. When using aluminum layers of either thickness with FS substrates, the exposure doses needed to be decreased to obtain similar diameters of dots as with aquaSAVE layers. An example is shown in Fig. 8, which presents an array of dots in PMMA with a 10 nm aluminum layer, fabricated with a lower dose than in Fig. 1. The diameters of dots decreased as one could expect; yet, they are larger than predicted numerically for this dose regime (see Fig. 7).

In the case of 10 nm aluminum coated PMMA on silicon substrates, as seen in Fig. 9, the measured dot diameters

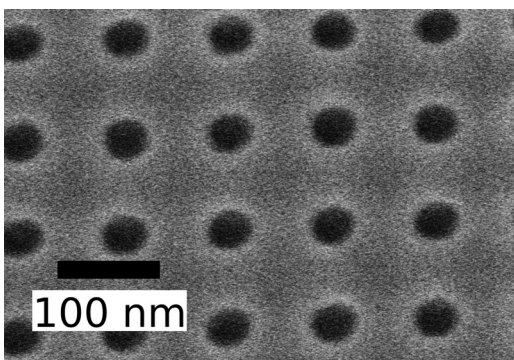


Fig. 8. SEM image of dots with a 100 nm pitch fabricated in PMMA resist on fused silica substrate with evaporated 10 nm aluminum film exposed at 30 keV voltage with 6 fC/dot dose and developed for 20 s in IPA:H₂O (7:3) at room temperature.

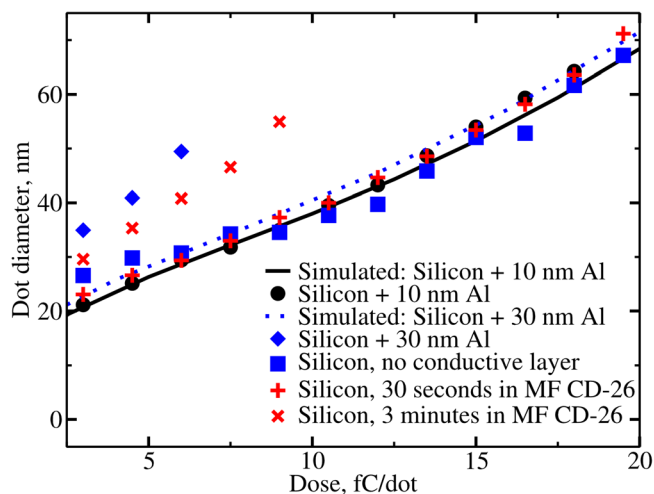


Fig. 9. (Color online) Comparison of dot sizes for 100 nm pitch dot arrays in 100 nm thick PMMA for a range of exposure doses on silicon, using a 30 keV accelerating voltage and 100 nm pitch dots with a 20 s development in IPA:H₂O (7:3). Lines correspond to simulated results and symbols correspond to experimental data. Results marked with an x represent a silicon sample with no aluminum layer and developed after being placed in the aluminum etchant MF CD-26 for 3 min.

were smaller than on FS substrates and they agreed well with simulations. Such experiments also gave highly uniform dot arrays in the resist as seen in Fig. 1(e). In this case, the dot diameters were also similar to those obtained on silicon substrate without conductive layers [Fig. 1(f)] as well as with conductive polymer layers [Fig. 1(d)]. Samples with 30 nm thick aluminum layers, however, showed roughened edges when exposed with high doses as well as enlarged widths, resulting in narrower applicable dose windows in comparison with 10 nm films. Figure 10 shows an example of pattern degradation observed at an edge of the applicable dose window using a 30 nm thick Al film.

The discrepancy between simulation and experiment for 10 nm aluminum-coated PMMA on fused silica substrates, but not on silicon substrates, may be tentatively attributed to a slight charge build-up remaining after application of the aluminum thin film. Lower conductivity of 20 nm and

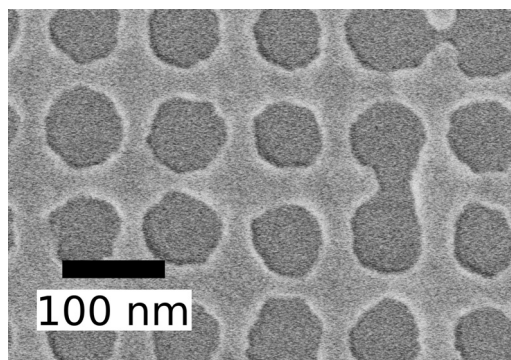


Fig. 10. SEM image of dots with a 100 nm pitch fabricated in PMMA resist on silicon substrate with evaporated 30 nm thick aluminum film exposed at 30 keV voltage with 7.5 fC/dot dose and developed for 20 s in IPA:H₂O (7:3) at room temperature.

thinner aluminum layers, compared to 30 nm films, was observed using SEM imaging of our samples prior to exposure. In Fig. S6(a) (supplementary material), a charge build-up can be seen for a sample with a 20 nm Al film on a fused silica substrate. However, no sign of charging was observed with 30 nm thick aluminum films [Fig. S6(b)]. SEM images of cleaved samples with 30 nm aluminum layer confirmed the continuous coverage (see Fig. S7). This is consistent with published data for other metals such as silver, gold, copper, and iron where conductivity has been shown to sharply decrease for metal film thicknesses below 20 nm.²⁵ Generally, lower conductivity of thin metal films compared to thicker layers has been attributed largely to the nonuniform nucleation in the deposited film.²⁶ Another possible explanation has been the oxidation of the thin aluminum films.²⁷

The described charge buildup arguments do not explain the observed difference of measured and predicted dot diameters employing 30 nm thick aluminum layers, since such layers do not show a sign of charging, while exhibiting an enlarged dot diameter with both fused silica and silicon substrates. Elsewhere the effects of the aluminum etchant on PMMA causing poor adhesion have been reported.^{28,29} To investigate the influence of the aluminum etchant on the observed morphology, samples of PMMA on silicon with no aluminum layers were treated by the etchant for different durations before EBL processing (see Fig. 9). Etching of samples for 30 s showed no effect on the development of the holes. As seen in Fig. 9, these samples produced similar results to other samples with accurately predicted dot diameters. Longer etch times of 3 min, however, created significantly larger dot sizes and a narrow dose range before collapse between dots occurred for dot doses above 9 fC (Fig. 10), indicating that PMMA resist performance is significantly altered by the etchant. Large increases of dot size in samples treated by etchant for long etch times of 3 min, both with and without aluminum coatings, suggest that the overlying aluminum layer offers limited protection to the resist from the aluminum etchant. Overall, the aluminum etching seems to negatively affect the EBL process for aluminum layers thicker than 10 nm where longer etch times are required.

Table I summarizes the comparison of predicted and measured dot diameters in the various samples considered. As discussed, we observe a reasonable agreement of simulations with the experiments in the cases of aquaSAVE coated

PMMA on both fused silica and silicon substrates, in the case of 10 nm aluminum coated PMMA on a silicon substrate, and also in the case of uncoated PMMA resist on a silicon substrate. For 10 nm aluminum coated PMMA on a fused silica substrate, as well as for 30 nm aluminum coated PMMA on either substrate, the predicted dot diameters are smaller than observed. As described in Sec. III, two main assumptions were made in our model, that travel of electrons at the exposure stage is not influenced by charge build-up, and that the conductive layer can be removed without influencing the development of exposed PMMA. According to our findings, both assumptions appear satisfied for polymer-coated PMMA, but not necessarily for aluminum-coated PMMA. In the latter case, the data available to us suggest that two different factors, an influence of charge buildup and an impact of aluminum etchant, might have contributed for 10 nm and 30 nm Al layers, respectively.

V. SUMMARY AND CONCLUSIONS

EBL nanopatterning of PMMA resist on dielectric fused silica substrates employing anti-charging layers of aluminum and conductive polymer, aquaSAVE, was investigated. In particular, arrays of dots with a 100 nm pitch were fabricated in PMMA. Patterning of similar multilayer systems on semi-conducting silicon substrates was also reported for comparison. An EBL simulation tool reported earlier^{13,14} was extended to incorporate electron beam widening from anti-charging layers on top of the resist. Simulations of exposure and development of the arrays of dots in PMMA on SiO₂ and silicon substrates, with various anticharging layers, were performed and the resulting development patterns compared with the experiments.

The aquaSAVE conductive polymer was found to enable high resolution patterning on fused silica substrates, where a good agreement between the corresponding experiments and simulations was observed. Good quality patterning was also seen on samples incorporating both 10 nm and 30 nm thick aluminum conductive layers; however, the dot sizes were larger than observed compared with aquaSAVE layers at similar process conditions. Increased thicknesses of aluminum layers led to even larger features and smaller applicable dose windows. Simulations for aluminum layers on fused silica substrates showed consistently smaller feature sizes compared to experimental results. Charge build-up in the case of thin aluminum coatings and the influence of aluminum etchant with thicker layers were both seen to be plausible causes of feature size increases. In particular, benchmark experiments with PMMA samples on silicon substrates with no aluminum layers, exposed to the etchant showed enlarged features and significantly reduced applicable dose windows.

Overall, the results presented highlight the importance of thorough comparative analyses of various anticharging schemes involving bench-testing against various model assumptions in order for the many dimensions of the ultra-high resolution EBL nanopatterning to be fully understood and rationally optimized.

TABLE I. Summarized comparison of measured and predicted dot sizes in coated and uncoated PMMA resist on fused silica and silicon substrates. Here, “+” means agreement and “-” indicates a discrepancy. In the last cases, hypothetical factors that might have caused the difference are indicated based on the available data.

Substrate	Conductive layer			
	AquaSAVE	10 nm Al	30 nm Al	No layer
Fused silica	+	-Charge buildup	-Al etchant damage	N/A
Silicon	+	+	-Al etchant damage	+

ACKNOWLEDGMENTS

This work was supported by the Natural Sciences and Engineering Research Council of Canada, nanoBridge, the National Research Council of Canada, and the National Institute for Nanotechnology (NRC-NINT). The authors would also like to thank the nanoFAB staff at the University of Alberta for their assistance.

- ¹A. J. Ikushima, T. Fujiwara, and K. Saito, *J. App. Phys.* **88**, 1201 (2000).
- ²C. Jeppesen, S. Xiao, N. A. Mortensen, and A. Kristensen, *Opt. Commun.* **284**, 799 (2011).
- ³D. Xia, D. Yan, and S. Hou, *Small* **8**, 2787 (2012).
- ⁴M. Graczyk, M. Balaz, A. Kvennefors, H. Linke, and I. Maximov, *J. Vac. Sci. Technol. B* **30**, 06FF09 (2012).
- ⁵M. Fan, G. F. Andrade, and A. G. Brolo, *Analytica Chimica Acta* **693**, 7 (2011).
- ⁶S. Roy and Z. Gao, *Nano Today* **4**, 318 (2009).
- ⁷P. Rodríguez-Franco, A. Arriola, N. Darwish, J. Jaramillo, H. Keshmiri, T. Tavera, S. Olaizola, and M. Moreno, *Sens. Actuators B* **187**, 356 (2013).
- ⁸P. Voisin, M. Zelsmann, C. Gourgon, and J. Boussey, *Microelectron. Eng.* **84**, 916 (2007).
- ⁹K. M. Satyalakshmi, A. Olkhovets, M. G. Metzler, C. K. Harnett, D. M. Tanenbaum, and H. G. Craighead, *J. Vac. Sci. Technol. B* **18**, 3122 (2000).
- ¹⁰Y. Todokoro, A. Kajiya, and H. Watanabe, *J. Vac. Sci. Technol. B* **6**, 357 (1988).
- ¹¹B. Samantaray and J. T. Hastings, *J. Vac. Sci. Technol. B* **26**, 2300 (2008).
- ¹²H. Demers, N. Poirier-Demers, A. R. Couture, D. Joly, M. Guilmain, N. de Jonge, and D. Drouin, *Scanning* **33**, 135 (2011).
- ¹³M. Stepanova, T. Fito, Z. Szabó, K. Alti, A. Adeyenuwo, K. Koshelev, M. Aktary, and S. Dew, *J. Vac. Sci. Technol. B* **28**, C6C48, (2010).
- ¹⁴K. Koshelev, M. Ali Mohammad, T. Fito, K. L. Westra, S. K. Dew, and M. Stepanova, *J. Vac. Sci. Technol. B* **29**, 06F306, (2011).
- ¹⁵S. Johnson *et al.*, *Microelectron. Eng.* **67**, 221 (2003).
- ¹⁶K. Lim, J. S. Wi, S. W. Nam, S. Y. Park, J. J. Lee, and K. B. Kim, *Nanotechnology* **20**, 495303 (2009).
- ¹⁷T. C. Bailey *et al.*, *Microelectron. Eng.* **61**, 461 (2002).
- ¹⁸M. Muhammad, S. C. Buswell, S. K. Dew, and M. Stepanova, *J. Vac. Sci. Technol. B* **29**, 06F304 (2011).
- ¹⁹C. A. Schneider, W. S. Rasband, and K. W. Eliceiri, *Nature Methods* **9**, 671 (2012).
- ²⁰M. Aktary, M. Stepanova, and S. K. Dew, *J. Vac. Sci. Technol. B* **24**, 768 (2006).
- ²¹M. A. Mohammad, T. Fito, J. Chen, S. Buswell, M. Aktary, M. Stepanova, and S. K. Dew, *Microelectron. Eng.* **87**, 1104 (2010).
- ²²W. T. Scott, *Phys. Rev.* **76**, 212 (1949).
- ²³D. Liljequist, F. Salvat, R. Mayol, and J. D. Martinez, *J. Appl. Phys.* **65**, 2431 (1989); D. Liljequist, F. Salvat, R. Mayol, and J. D. Martinez, *ibid.*, Erratum **66**, 2768 (1989).
- ²⁴See supplementary material at <http://dx.doi.org/10.1116/1.4827813> for additional and more comprehensive simulation and experimental results.
- ²⁵I. Antonets, L. Kotov, S. Nekipelov, and E. Karpushov, *Techn. Phys.* **49**, 1496 (2004).
- ²⁶M. Ohring, *Materials Science of Thin Films*, 2nd ed. (Academic, San Diego, 2002).
- ²⁷C. Aumann, G. Skofronick, and J. Martin, *J. Vac. Sci. Technol. B* **13**, 1178 (1995).
- ²⁸E. Dobisz, <http://www.researchgate.net> at <http://goo.gl/OWxBFS>.
- ²⁹S. L. Holl, C. A. Colinge, S. Song, R. Varasala, K. Hobart, and F. Kub, *ECS Trans.* **3**, 67 (2006).